applied sciences

MDPI

Article

Computed Tomography-Driven Design and Fused Filament Fabrication of Graded Density Bone Scaffolds

Luca Grigolato and Gianpaolo Savio *

Department of Civil, Environmental, and Architectural Engineering, University of Padova, Via Venezia 1, 35131 Padova, Italy; luca.grigolato@unipd.it
* Correspondence: gianpaolo.savio@unipd.it

Featured Application: The work finds potential application in the design and manufacture of patient-specific scaffolds in the biomedical field using desktop MEX AM technologies.

Abstract: The design of scaffolds and prostheses benefits from the opportunities provided by additive manufacturing technologies. Specifically, scaffold design using cellular structures based on lattices has become a significant focus. These lattice-based scaffolds exhibit intricate and complex shapes with controlled macro-porosity. In this study, a method is presented that enables the modeling of a graded-density lattice structure for material extrusion additive manufacturing, without relying on a geometric lattice model. The methodology utilizes computed tomography (CT) scans as inputs to obtaining a 3D scalar field and a surface model. The lattice structure is designed and generated within the computer-aided manufacturing (CAM) software, ensuring consistent machine toolpaths. The 3D scalar field, representing a relative density map derived from CT Hounsfield units, drives the variation of the extrusion parameters generated by the CAM, achieving a graded-density lattice. To demonstrate the effectiveness of the method, a section of a human femur bone with a lattice with a triply periodic minimal surface (TPMS) gyroid pattern was designed and 3D-printed, replicating the relative density of the target tissue.

Keywords: volumetric modeling; graded lattices; functionally graded lattice structures; computed tomography; fused filament fabrication; additive manufacturing

Academic Editor: Marek Placzek

Received: 25 April 2025
Revised: 3 June 2025
Accepted: 4 June 2025
Published: 7 June 2025

Citation: Grigolato, L.; Savio, G. Computed Tomography-Driven Design and Fused Filament Fabrication of Graded Density Bone Scaffolds. *Appl. Sci.* **2025**, *15*, 6434. https://doi.org/10.3390/app15126434

1. Introduction

Tissue engineering and regenerative medicine are interdisciplinary fields that have undergone significant advancements in recent decades. These fields aim to develop biological and synthetic substitutes that replicate the structure and function of natural tissues. The conventional method is the autograft method but it is not always feasible, mainly due to the availability of donor tissues [1]; therefore, the adoption and demand for artificial substitutes are increasing [2].

In this context, two different strategies are commonly employed, involving prostheses and scaffolds. Prostheses are permanent or semi-permanent artificial devices designed to restore the structural or functional role of damaged tissues or organs. They are typically fabricated from biocompatible materials such as titanium, ceramics, or high-strength polymers and do not actively promote tissue regeneration.

Scaffolds, by contrast, are temporary, porous, interconnected structures designed and engineered to enhance cellular interactions, mimicking the extra-cellular matrix [3]. They

support cell attachment, proliferation, and tissue regeneration, and are biodegradable, gradually degrading as the natural tissue forms and replaces the scaffold.

Among the traditional methods for producing scaffolds—such as electrospinning, soluble solid templating, the decellularization of natural tissues, particulate leaching, gas foaming, sintering, and freeze-drying—additive manufacturing (AM) has emerged as an approach that can overcome the limitations of these methods, allowing full engineering of the final scaffolds [1,4].

Since scaffolds must have specific characteristics related to the biological aspect, structure, and chemical composition, AM seems the perfect approach for their production. AM enables high customization to match the patient-specific anatomy, precise control over the internal architecture and porosity, and an ever-growing range of available materials. These include materials such as synthetic polymers (e.g., polylactic acid (PLA), polyglycolic acid (PGA), polycaprolactone (PCL)) and natural polymers (e.g., collagen, fibrin, chitosan and glycosaminoglycans (GAG)), or bioceramics (e.g., hydroxyapatite (HA), β-tricalcium phosphate (β-TCP), α-TCP, calcium silicate, bioactive glasses) and hybrid materials [1,2,5–8]. For protheses, metals are often used, such as pure titanium, Ti6Al4V alloys, stainless steel AISI 316L, cobalt–chromium, and cobalt–chromium–molybdenum (especially used in dental prosthetics), as well as magnesium alloys such as Mg-Ca-Zn. The common AM technologies used in scaffold fabrication include selective laser sintering (SLS), material extrusion (MEX), and vat photopolymerization (VPP) [1,4].

Enabling the AM workflow, patient-specific scaffolds can be designed based on biomedical imaging techniques such as CT or magnetic resonance imaging (MRI), and their internal architecture and porosity are engineered and customized using computer-aided manufacturing (CAD) software.

1.1. Computed Tomography and Hounsfield Units

CT is one of several medical imaging techniques based on tomography, alongside MRI and positron emission tomography (PET), all of which are used in radiology for diagnostic purposes by producing cross-sectional images of the internal anatomy. Unlike MRI or PET, CT relies on X-rays to acquire image data.

A CT scan results in a volumetric model composed of a stack of two-dimensional images, where the pixel values (scalars) are stored in a regular voxel-based data structure. Each voxel's pixel value corresponds to a specific property measured by the scanner and then converted into a CT number.

DICOM (digital imaging and communication in medicine) is the internationally recognized standard for the digital storage and transmission of medical images. It was developed by the American College of Radiology (ACR) and the National Electrical Manufacturers Association (NEMA) [9,10].

In DICOM standards, the conversion units—known as the rescale type—are specified in the metadata tag {0028,1054}. Pixel values can be converted into meaningful units using one of two methods: rescale slope and intercept (tags {0028,1052} and {0028,1053}), typically used when the relationship is linear, where the values of the slope and intercept are device-specific and provided by the hardware manufacturer; lookup table (LUT) (tag {0028,3000}), used when the conversion relationship is nonlinear.

CT numbers are most commonly expressed in Hounsfield units (HUs), a relative quantitative measure of radiodensity widely used in clinical interpretation [11]. However, the limitations and inconsistencies of HUs as absolute values have been known since the early days of CT [12]. HU values are proportional to the linear attenuation coefficient μ (cm^{-1}) of a material, which depends on the effective photon energy E (keV). In practical

terms, HU values represent CT attenuation normalized to the reference values of water $_{water}$ and air μ_{air}:

$$HU = \left(\frac{\mu - \mu_{water}}{\mu_{water} - \mu_{air}} \right) \cdot 1000$$

which are 0 and −1000 by definition, respectively [13]. It also possible to obtain HU values vs. physical density ρ curves [14,15].

1.2. Design Methods of Scaffolds for AM

The design and manufacturing of scaffolds are guided by specific mechanical, biological, and physicochemical requirements [2]. Scaffolds are engineered to promote desirable cellular interactions, thereby supporting the formation of new functional tissues. Additionally, factors such as the interconnectivity, pore shape, pore size, surface area, mechanical strength, and degradation rate must be carefully considered to ensure compatibility with the surrounding tissue [16,17]. In this sense, the porosity and its complementary quantity, the relative density (or volumetric fraction), play a fundamental role in determining the mechanical (as described in the well-established Gibson and Ashby models [18]) and biological performance of scaffolds [19].

Lattice structures are a viable solution for the realization of customized scaffolds (or even porous prostheses) with tailored properties based on porosity [19,20]. The macro-porosity is geometrically modeled in CAD software but the meso- to micro-porosity can be obtained during the AM process or even in post-processing operations [21].

Lattice structures combined with AM allow for the multi-level customization of the geometry, material properties, and manufacturing parameters. Geometric customization involves tuning the unit cell shape, size, and relative density [20,22]; material customization can be achieved by modifying the micro-structure or using multi-material strategies to create functionally graded scaffolds; process parameters are customized to tune the final structure's properties. For example, in fused filament fabrication (FFF), factors such as the temperature and printing speed impact the flow rate, dimensional accuracy, interlayer adhesion, and anisotropy.

One of the main classification criteria is based on the type of lattice structure, being either beam-based (or strut-based) or surface-based (or sheet-based). The former includes structures such as cubic, octet, and similar lattices, while the latter comprises TPMS structures, including gyroid, p-surface, and other lattices [23]. For bone-substitute applications, TPMS structures are known to present some advantages over strut-based lattices [24].

Several geometric modeling approaches for lattice structures exist, some of which have been widely adopted and are now integrated into commercial software solutions such as nTopology, Materialise 3-matic, Autodesk Fusion 360, ANSYS Additive Suite, Siemens NX, and various addons for Grasshopper/Rhinoceros [2,19].

1.3. Previous Works

Numerous studies in the literature highlight the advantages of lattice structures produced with AM for medical applications [8,24–26].

Numerous researchers have explored the manufacturability of various lattice architectures and porosity levels. For example, Van Bael et al. [27,28] analyzed manufacturing deviations in metal lattices, focusing on the pore size, strut thickness, porosity, and surface area.

In parallel, other studies have investigated the mechanical behavior of different lattice configurations. Zhang et al. [29], for instance, examined complex strut-based lattice structures with spatially varying porosities designed to replicate the stiffness of distinct bone regions, such as cortical bone, the transition zone, and bone marrow.

The influence of geometric parameters—particularly the pore size and lattice cell dimensions—on osseointegration performance has also been widely studied. Warnke et al. [30] assessed the impact of pore sizes ranging from 450 to 1200 μm on osteoblast proliferation, noting that pores smaller than 600 μm facilitated complete tissue ingrowth. Taniguchi et al. [31] extended this investigation under in vivo conditions, evaluating the effect of the pore size on the interfacial strength between the bone and implant. They identified 600 μm pores as being optimal for long-term bone ingrowth and the development of robust bone–implant union. Similarly, Fukuda et al. [32] reported that porous channels of 500 μm offered the most favorable osseointegration outcomes within the tested range of 500–1200 μm. A similar pore size range was reported by Barba et al. [24], who observed that initial osteoblast cell colonization is enhanced by smaller pores, with faster colonization occurring when the pore sizes are below 600 μm. However, the effective vascularization of pre-bone tissue requires larger pores—greater than 300 μm—to accommodate blood vessel ingrowth. The lower pore size limit is also constrained by the specific combination of material and AM technology employed, as smaller pores may lead to powder entrapment and pore occlusion.

Others have explored the use of biocompatible polymers. Guo et al. [33] fabricated biomimetic HA scaffolds with TPMS structures using desktop-scale digital light processing (DLP), achieving improved degradation behavior and enhanced biological performance through process optimization. Similarly, Zhang et al. [34] developed 3D-printed poly-l-lactic acid (PLLA)–nano-hydroxyapatite (nHA) scaffolds with a high nHA content of up to 50% using FFF. These scaffolds exhibited a compressive strength of 14.2 MPa, which is comparable to that of human cancellous bone (2–12 MPa).

A very similar approach to the one presented in this work was proposed by Okkalidis [35]. He presented a method that employs CT scans to construct patient-specific phantoms by controlling the filament extrusion rate in FFF technologies.

Most recently, Yau et al. [36] developed a heterogeneous scaffold by integrating medical imaging data with the octree-based adaptive subdivision technique. The scaffold was manufactured using selective laser melting (SLM) with a biocompatible Ti6Al4V alloy.

1.4. Aim

This work addressed the design and additive manufacturing of graded porous scaffolds based on CT scans HU values, aiming to tune the relative density of lattice structures by controlling the filament extrusion amount during deposition in order to replicate the tissue's native porosity.

CAD modeling operations were used for the macro-shape design via B-rep modeling, while CAM software supported the infill generation, enabling the creation of straightforward lattice structures. Additionally, CAD volumetric tools were employed in processing the CT scan 3D scalar field and editing the G-code. Compared to previous studies, this approach bypasses the need for the complex geometric modeling of graded lattice structures, avoiding both implicit or B-rep representations, which opens new possibilities for scaffold design and manufacturing. The main innovations of this work lie in the novel integration of medical imaging data with FFF to create graded porous scaffolds. While considerations regarding the mechanical properties and biological experimentation fell outside the scope of the present work, they are nonetheless discussed throughout the paper.

This paper is organized as follows. Section 2 describes the proposed methodology and its implementation, while Section 3 presents a case study focused on a femur bone segment, followed by a discussion of the results and the identified limitations.

2. Materials and Methods

Figure 1 shows the workflow of the proposed design method. A CT scan serves as the input for the workflow. The HU values are extracted from the CT scan and a voxel model (i.e., a 3D scalar field, which is a grid of values (voxels) representing the scalar quantity at each point in space) is constructed replicating the data structure dimensions. The volumetric HU scalar field is segmented to obtain a discrete surface model of the biological tissue under investigation. The discrete surface model is utilized to compute the numerical control file, called G-code, for a specific FFF machine. In this step, the lattice structure is also modeled by setting process parameters such as the infill pattern and density. The voxel model is remapped from HU to relative density values. Then, the relative density 3D scalar field is moved and oriented on the FFF machine reference frame and the G-code is consequently modified based on the required relative density. Finally, the modified G-code is executed on the specific FFF 3D printer, allowing the fabrication of a graded-density component.

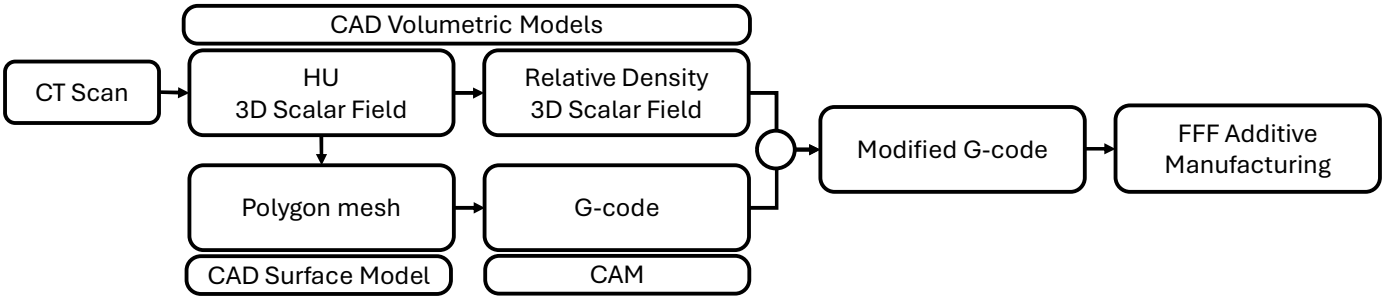

Figure 1. Workflow schematic.

The whole methodology is implemented in Rhinoceros 8 (McNeel and Associates, Seattle, WA, USA) and its plugin Grasshopper environment using a combination of existing addons, including Monolith (release 0.3.6415.29557, Autodesk Inc., San Francisco, CA, USA), as well as custom Python scripts (Python 3.9) with external libraries such as pydicom for DICOM file manipulation and NumPy. The G-code file for the FFF 3D printer is computed with Slic3r 1.30 [37]. A Creality CR-10 Smart Pro printer (Shenzhen Creality 3D Technology Co., Ltd., Shenzhen, China) equipped with a Creality Sprite Pro extruder (direct drive), and a 0.4 mm MK8 steel nozzle is used for manufacturing the part. Here, PLA was chosen as the material for its availability and biocompatibility and biodegradability properties [38].

2.1. CAD

This section describes the steps involving CAD modeling for volumetric and surface entities.

2.1.1. Volumetric Models

The CT scan data are stored as DICOM files. The volumetric HU 3D scalar field is read from the DICOM file as a voxel model data structure. The voxel model is defined by the number and size of elements in the X, Y, and Z directions, along with pixel data for each element. The information, related to the voxel model data structure, is stored as metadata in the DICOM file header. Here, tag {0028;0011} defines the number of columns, i.e., number of voxels in the X direction (nX), while tag {0028;0010} defines the number of rows, i.e., the number of voxels in the Y direction (nY), and the number of voxels along the Z direction corresponds to the number of acquisitions (nZ), with attribute {0020;0013} being the "instance number". The voxel sizes (vS) are saved in the attribute {0028;0030} as

"pixel spacing" for the XY dimensions (vSX, vSY), while the Z dimension can be found in the attribute {0018;0050} as the slice thickness (vSZ). The rescale slope and intercept values and type are checked and applied to retrieve the correct HU values from the images.

Attribute {0020;0032} for the "image position (patient)" defines the x, y, and z coordinates of the center of the first voxel transmitted relative to the scanner table reference frame, while the orientation is defined in tag {0020;0037} for the "image orientation (patient)" and eventually used to correctly rotate the volumetric model with respect to the printing direction.

Once the HU 3D scalar field is reconstructed, correctly positioned, oriented, and visualized in the 3D space, the user defines a region of interest (ROI) using a box. An ROI is a subset of the 3D scalar field, used to isolate and evaluate regions such as bones, organs, or lesions—allowing for measurements (e.g., density, volume, shape) or further image processing. This ROI is used in the following step to perform Boolean operations.

2.1.2. Surface Model

The surface model is a polygon mesh of the specific tissue. Firstly, the HU 3D scalar field is segmented using a value (isovalue) of the HU domain in order to select the target tissue. The choice of an appropriate isovalue is crucial for creating a geometric model that accurately represents the boundary of the target tissue. The literature reports the HU ranges for organs and tissues segmentation [12,39,40]. Then, the surface model is obtained using polygonization algorithms, in this case through the Marching Cubes algorithm [41]. Next, the previously defined box, i.e., the ROI, can be used to isolate the portion of tissue under investigation by performing Boolean operations on the polygon mesh.

2.2. CAM

This section describes the steps involving CAM software, which allows the design and modeling of the internal lattice structure. The CAM file, called the G-code for MEX FFF printers, can be prepared in a slicer software from the surface model.

2.2.1. Lattice Structure Design

As mentioned in the introduction, porosity design is a key element in scaffold engineering. The lattice structure is designed during G-code generation by choosing the infill type and infill density (ρ_s) and the lattice unit cell type to control the cell size [42]. The ρ_s can be calculated using the following function [42]:

$$\rho_s = \frac{k_c \cdot m}{L_{cell}} \left(1.25 \cdot \varphi + \left(\frac{\pi}{4} - 1\right) \cdot l_h\right), \quad (1)$$

where L_{cell} is the unit cell dimension in mm; the coefficient k_c depends on the infill type and is defined as the ratio between the average length of the toolpaths within a unit cell and the cell size L_{cell}; m, referred to as the multiplicity, is linked to the symmetry properties of the lattice unit cell and indicates the number of independent toolpaths per unit cell in a single layer; φ is the nozzle diameter in mm and l_h is the layer height in mm. The k_c and m values of three infill types, named gyroid, rectilinear, and 3D honeycomb, are reported in Table 1.

Table 1. Model coefficients for the considered infill types.

Infill Type	k_c	m
Gyroid	1.221	2
Rectilinear	0.707	2
3D Honeycomb	1.011	2

The ρ_s functions for the three types of infills we considered are shown in Figure 2. The different infill patterns were chosen due to their 3D geometries and to ensure interconnected porosity, particularly in the case of the rectilinear pattern (Figure 3).

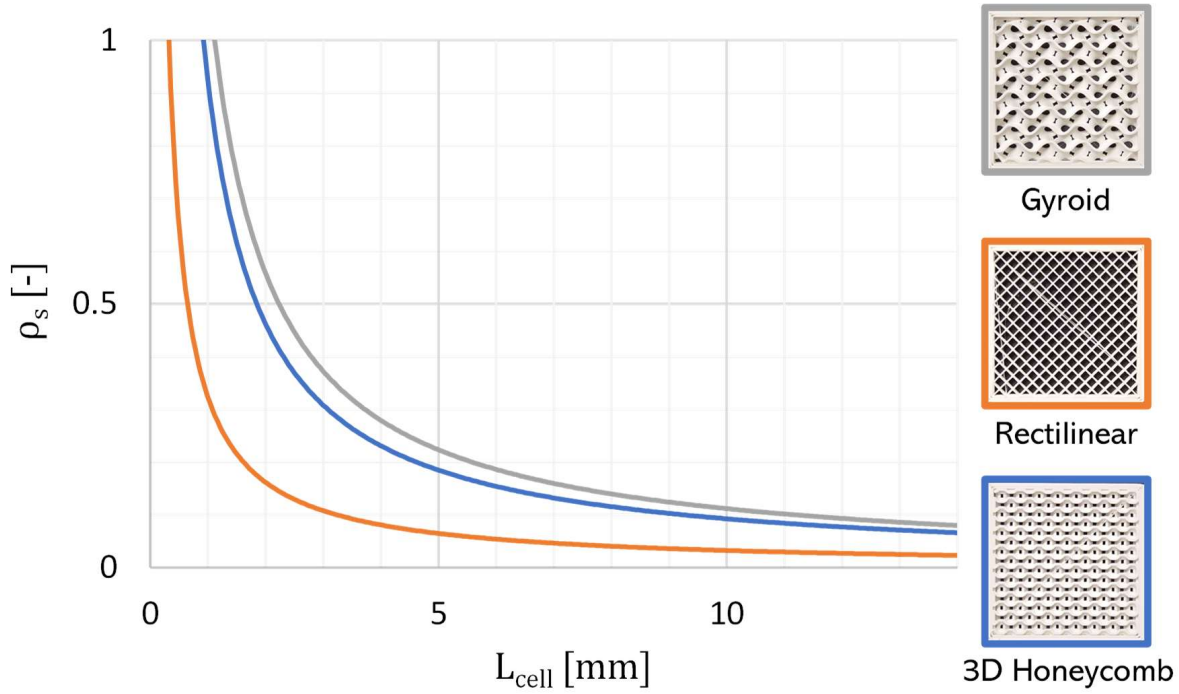

Figure 2. Graphical representation of the model for the infill patterns considered in the case of E_w = 0.4 mm, φ = 0.4 mm, and l_h = 0.2 mm.

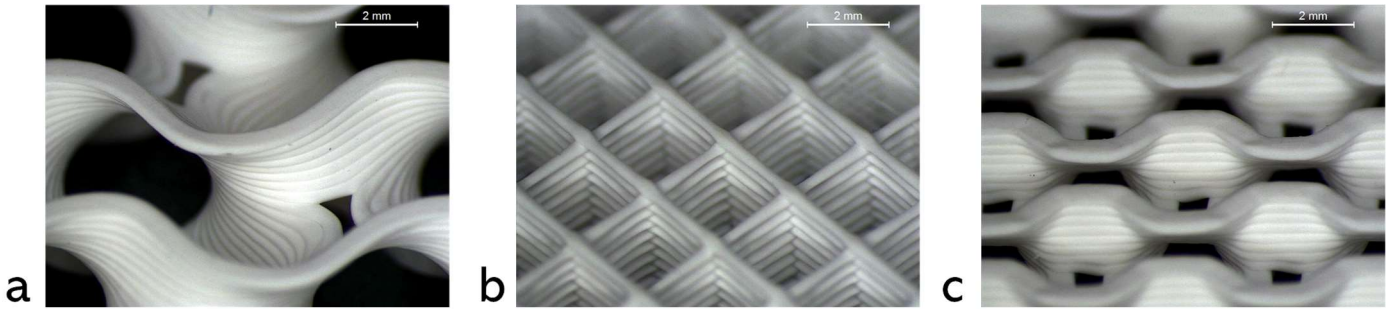

Figure 3. Close-up views of the gyroid (**a**), rectilinear (**b**), and 3D honeycomb (**c**) infill types, all printed at a constant setting of E_w = 0.4 mm. These images highlight the holes in the pattern that enable complete interconnectivity.

The L_{cell} should be chosen based on the infill type, model coefficients, maximum extrusion width E_w, and maximum relative density needed ρ, which is usually set to 1 to provide a fully solid structure.

The extrusion width E_w (Figure 4) has lower and upper limits $\left[E_{w,min}; E_{w,max}\right]$, which relate to the material, extrusion flow rate, nozzle diameter, temperature, viscosity, and print quality [42].

Considering the actual limits for part stability in the Z direction, $E_{w,min}$ can be approximated as:

$$E_{w,min} = l_h, \tag{2}$$

while $E_{w,max}$ can be approximated as:

$$E_{w,max} = 3\varphi. \tag{3}$$

For a constant l_h = 0.2 mm and a common nozzle diameter φ = 0.4 mm, $E_{w,min}$ and $E_{w,max}$ become 0.2 mm and 1.2 mm.

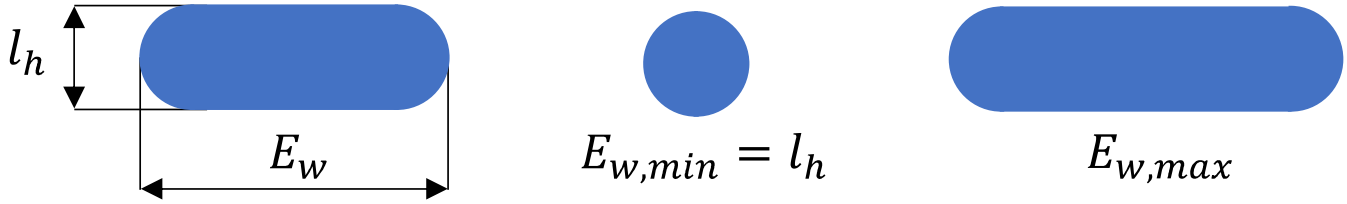

Figure 4. Bead section models.

Given the material, φ, l_h, and infill type, and consequently the $E_{w,min}$ and $E_{w,max}$, it is possible to compute L_{cell} as:

$$L_{cell} = E_{w,max} \cdot m \cdot k_c / \rho, \quad (4)$$

Therefore, the $E_{w,max}$ and infill type establish the optimal value of L_{cell}, and using Equation (1) or Figure 2, ρ_s could be determined.

It should also be considered that the maximum flow rate Q_{max} for a single material must be identified. One solution is to test the extrusion behavior for each pair of extrusion temperature T_{ext} and speed (feed speed v_{feed} or movement speed v_{sp}) values with a fixed nozzle (material and diameter) to understand if the material is extruded continuously or not [43,44].

2.2.2. Computer Numerical Control (CNC) Programming Language

Turning a digital design into a physical object requires defining and converting process parameters into machine instructions, which are then exported—most commonly—as G-code. G-code is a standardized and widely adopted language used to control machine operations such as movements, temperatures, and tool actions. It serves as the link between the virtual model and physical execution. Even though G-code is standardized (based on ISO 6983 [45]), there are many variants—such as Marlin, RepRap, and Fanuc—especially for FFF technologies, where these custom commands and syntax are specific to the machine firmware or controller.

In subtractive manufacturing, CAM software generates these instructions from settings such as the tool paths, cutting depths, and spindle speeds for CNC machines. In AM, so-called 'slicers' perform a similar role, using parameters such as the layer height, extrusion width, print speed, temperature, and many others to produce instructions for 3D printers. There are various slicing programs, many of which are free (such as Cura, PrusaSlicer, Slic3r, and OrcaSlicer) that process the 3D model, divide it into layers, and generate optimized G-code. These tools offer fine control over printing strategies, helping balance the quality, time, and material use.

2.3. CAD–CAM Integration

In this section, the CAD and CAM results are merged, since the CAM file is modified by the relative density scalar field and processed in a CAD environment. To generate and control the relative density gradient of the lattice structure, the extrusion amount is locally modified in the G-code file.

2.3.1. Alignment

Usually, the 3D scalar field and the G-code are not aligned in the Euclidian 3D space because the surface model, and consequently the resulting toolpath defined by G-code,

is placed in the printer bed in the slicer software, while the 3D scalar field is in its own reference frame.

To correctly transfer the 3D scalar field values to the G-code coordinates, they must be mutually aligned in the 3D space. The alignment can be achieved by roto-translating the 3D scalar field to the toolpath reference frame. Given that the polygonal mesh models are identical for both the CAM and the volumetric model, it is possible to compute the roto-translation by identifying the affine transformation that aligns the meshes. Moreover, in our case, the transformation is a simple translation and can be easily identified by the coordinates of a vertex of the bounding boxes.

The entities involved and their mutual positions are shown in Figure 5. The part of the bone under study was contained in a bounding box and placed in the 3D space within the volume occupied by the volumetric data. The origin of both the 3D scalar field and the toolpath was set at (0,0,0), while C_{v0} identifies the center of the first transmitted voxel.

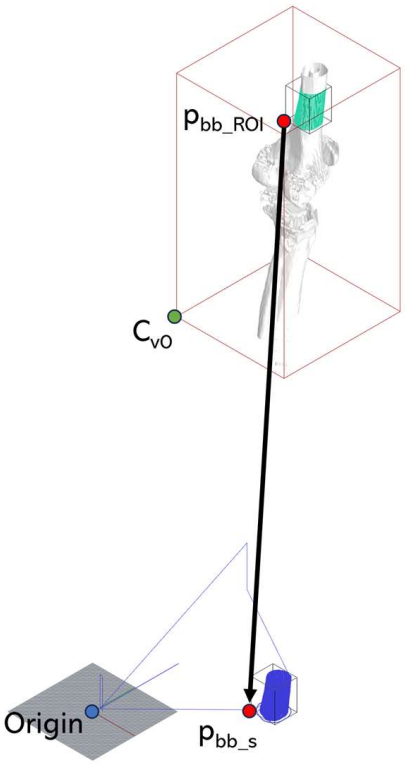

Figure 5. Visualization of the geometrical entities and translation vector, shown in black, adopted in the alignment of the toolpath onto the 3D scalar field. The toolpath is shown in blue. The dots indicate the key reference points, including the global origin (Origin, blue color), the center of the first transmitted voxel (C_{v0}, green color), a point on the bounding box of the surface model within the region of interest (p_{bb_ROI}) and its corresponding point (p_{bb_s}) on the bounding box of the surface model (and the toolpath), both in red color.

In the common case, if the ROI has faces parallel to the reference frame, no rotations are applied to either model, and the entire transformation is defined by the translation vector $\vec{v}$ (shown in black in Figure 5):

$$\vec{v} = p_{bb_s} - p_{bb\_ROI} \tag{5}$$

as the vector connecting the point of the surface model bounding box (p_{bb_ROI}) and the corresponding point (p_{bb_s}) on the surface model (and the toolpath) bounding box as positioned in the CAM software.

2.3.2. Conversion from HU Values to Relative Density Scalar Field

Depending on the anatomical site and factors such as age, sex, and pathologies, the scientific literature suggests that a healthy bone has a cortical porosity range of 5–15% and a physical density range of approximately 1.9–2.0 g/cm^3 [46–49]. Trabecular bone has a porosity range of 50% to 95%, with the same physical density range, while bone marrow has a physical density range of 0.98–1.1 g/cm^3 [46,48–51]. The typical HU values range from approximately 150 to 400 for trabecular bone, while the literature values for typical cortical bone suggest a range of 500 to 1800 HU [40,49].

By performing a Boolean intersection operation between the HU scalar field and the surface model, the voxels contained inside the surface model are selected. The HU minimum (HU_{min}) and maximum (HU_{max}) values of this subset found in the scientific literature, along with the porosity value $P = 1 - \rho$ for the specific bone tissues (trabecular bone P_{trab} and cortical bone P_{cor}), were adopted to derive a linear equation that maps HU values to P and then to relative density ρ values, as illustrated in Figure 6. Higher value of porosity can lead to part instability in the Z direction. To avoid this, P should be limited to $P_{E_{w,min}}$, which depends on the $E_{w,min}$, L_{cell}, and infill type model coefficients. By means of this correlation, it possible to calculate ρ associated with the HU values in the ROI.

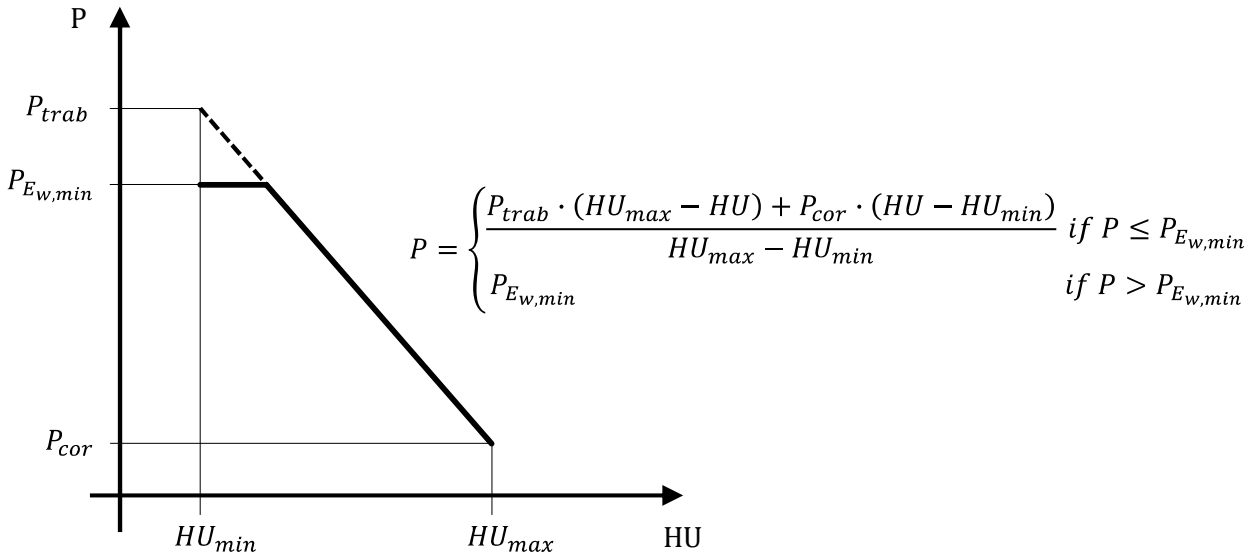

Figure 6. Representation of the linear equation that maps HU values to P values.

Other useful conversion methods of HU values are feasible, such as converting HU values to physical densities and elemental compositions, although they are not helpful in this context [52].

2.3.3. G-Code Editing

With the CAD and CAM models properly aligned, the G-code can be modified wisely. Since a G-code file consists primarily of motion instructions in the format of G1 Xx Yy Zz Ee, where X, Y, and Z represent the Cartesian coordinates and E specifies the extrusion length in mm for the filament feed, each $i - th$ position along the toolpath in the infill section is considered:

$$\Delta E_{e,i} = \Delta E_{s,i} \frac{\rho_{e,i}}{\rho_s}, \quad (6)$$

where $\Delta E_{e,i}$ represents the required material amount at the $i - th$ point of the toolpath in the G-code editing phase; $\Delta E_{s,i}$ is the material amount calculated by the slicer software, while ρ_{slicer} denotes the infill density from the slicing process. Additionally, $\rho_{e,i}$ is the required

relative density at the $i-th$ point obtained through trilinear interpolation of the ρ 3D scalar field onto the mid-point of each toolpath segment [53]. It must be noted that the voxel structure or volumetric model is employed as an interpolation grid, making the CT voxel size (vSX, vSY, and vSZ) independent of the scaffold's cell size L_{cell}.

The computation of $\Delta E_{e,i}$ incorporates the minimum relative density $\rho_{e,min} = 1 - P_{E_{w,min}}$ for a consistent part, considering the layer thickness l_h among the various parameters. To simplify the G-code editing and avoid calculating $\Delta E_{s,i}$, relative E coordinates are used instead of absolute coordinates. A custom Python script was developed to implement the G-code editing. The pseudocode is reported below:

```
for each line in the G-code file:
    if available, extract X, Y, Z, E
    if line is infill:
        calculate interpolated value ρe,I at X, Y, Z
        if ρe,I < ρemin:
            ρe,I = ρemin
    compute new value for E (Equation (6))
    substitute new value for E in G-code line in E position
```

3. Test Case and Discussion

To test the method functionalities, the implemented solution was used to generate a graded lattice from a femur bone section.

3.1. Preliminary Process Calibration

The maximum extrusion width, $E_{w,max}$, must be determined based on the specific extruder configuration and material characteristics, while $E_{w,min}$ = 0.2 mm, according to Equation (3) and a previous study [42]. For Amazon White PLA filament, the maximum flow rate reachable at T_{ext} = 215 °C with the adopted hardware (Sprite Extruder with φ = 0.4 mm) is Q_{max} = 19.24 mm^3/s. This value corresponds to the threshold beyond which the stepper motor begins to lose steps, indicating that a continuous material flow can no longer be maintained.

Extrusion tests were carried out at various feed rates (F = 500, 1500, 3000, and 5000 mm/min), corresponding to the movement speed v_{sp} (mm/s), and at different target extrusion widths (E_w = 0.5, 1.2, 1.5, and 2 mm), all at T_{ext} = 215 °C. The quality of the deposition was evaluated by analyzing the actual E_w dimensions and the retention of the bead shape over a cross-section of 20-layer, single-bead samples.

For every F, at E_w = 0.5 mm, the shape of the beads is retained (one example is shown in Figure 7a), and at E_w = 2 mm the bead shape is not retained (Figure 7d). For E_w = 1.2 and 1.5 mm (Figure 7b,c), tested only at 1500 mm/min, the shape is reasonably preserved but the actual E_w is lower than the designed one in the first layers (1.02 and 1.16 mm). After a few layers, however, the deposition becomes misaligned with the vertical direction and the beads are deposited on top of each other, resembling the designed E_w, with a measured width of 1.37 and 1.66 mm. This behavior is more pronounced at higher F values, where misalignments in the upper layers occur, likely due to increased vibrations in the printer frame (or extruder) during deposition or flow instabilities [43]. Moreover, at E_w = 2 mm, visible underextrusion can be observed because the Q_{max} limit was reached. Therefore, at T = 215 °C, F values up to 1500 mm/min are suitable to reduce bead misalignment, while $E_{w,max}$ should fall within the range of 1.2–1.5 mm. The approximation for $E_{w,max}$ previously described in Equation (4) can also be used.

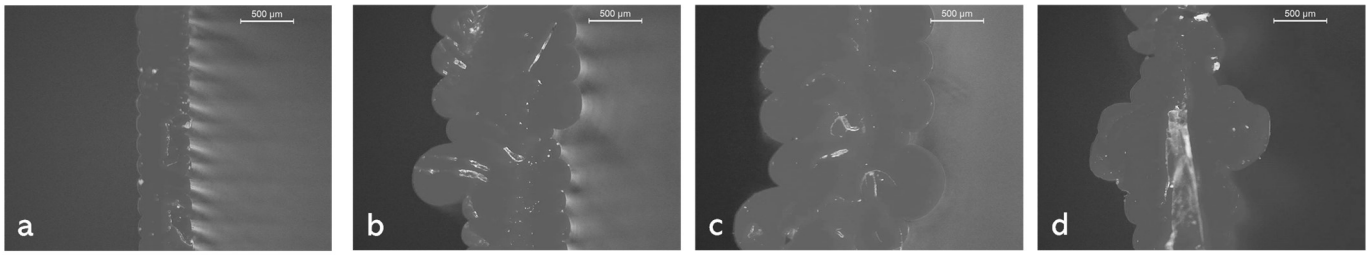

Figure 7. Sections of the samples: E_w-F = 0.5-1500 (**a**); 1.2-1500 (**b**); 1.5-1500 (**c**); 2-5000 (**d**).

3.2. Femur Segment

The methodology has been applied to the creation of a femur bone portion. The anonymized CT scan of a knee is available in an online repository [54]. Table 2 provides the CT properties for the volumetric data structure. The rescale slope and intercept values were set to 0.0 and 1.0, while the rescale type was the HU. The HU values ranged from −1000 to +1562. No information regarding the photon energy (E) was reported in the metadata. The first voxel center C_{v0} was at X = −9.80818 mm, Y = 148.609 mm, Z = 488.571 mm.

Table 2. CT volumetric data structure properties.

Direction	Data Structure Size n	Voxel Size vS
X	182	0.976562 mm
Y	197	0.976562 mm
Z	107	3.27 mm

Based on the HU values reported in the literature, the HU 3D scalar field was segmented using a threshold of 350 HU (Figures 8 and 9).

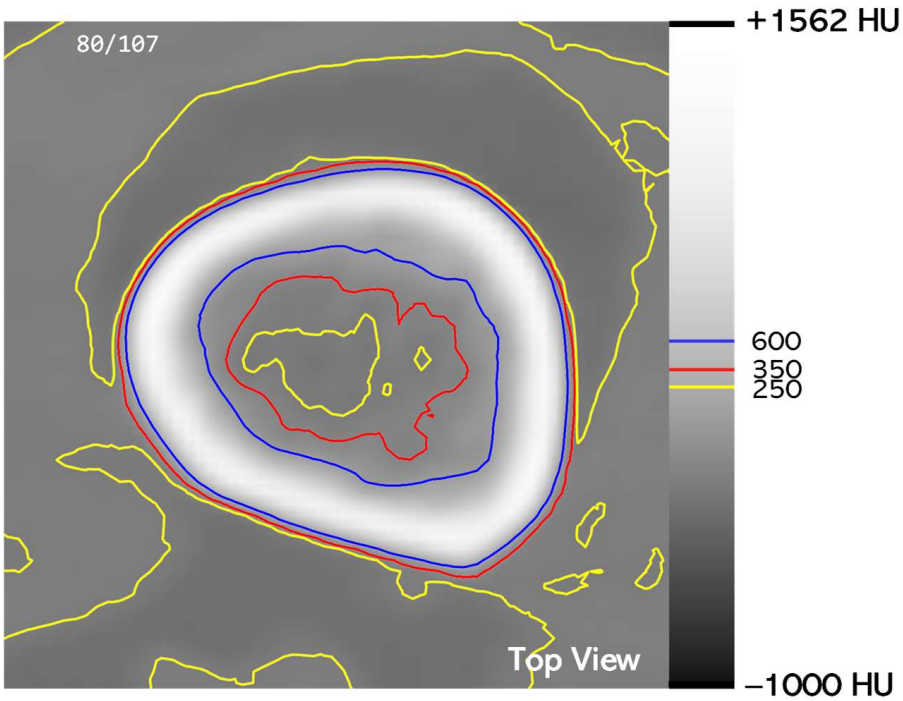

Figure 8. Visualization of the isocurves for the isovalues at HU = 250 (yellow), 350 (red), and 600 (blue) on top of the corresponding CT slice in grayscale colors.

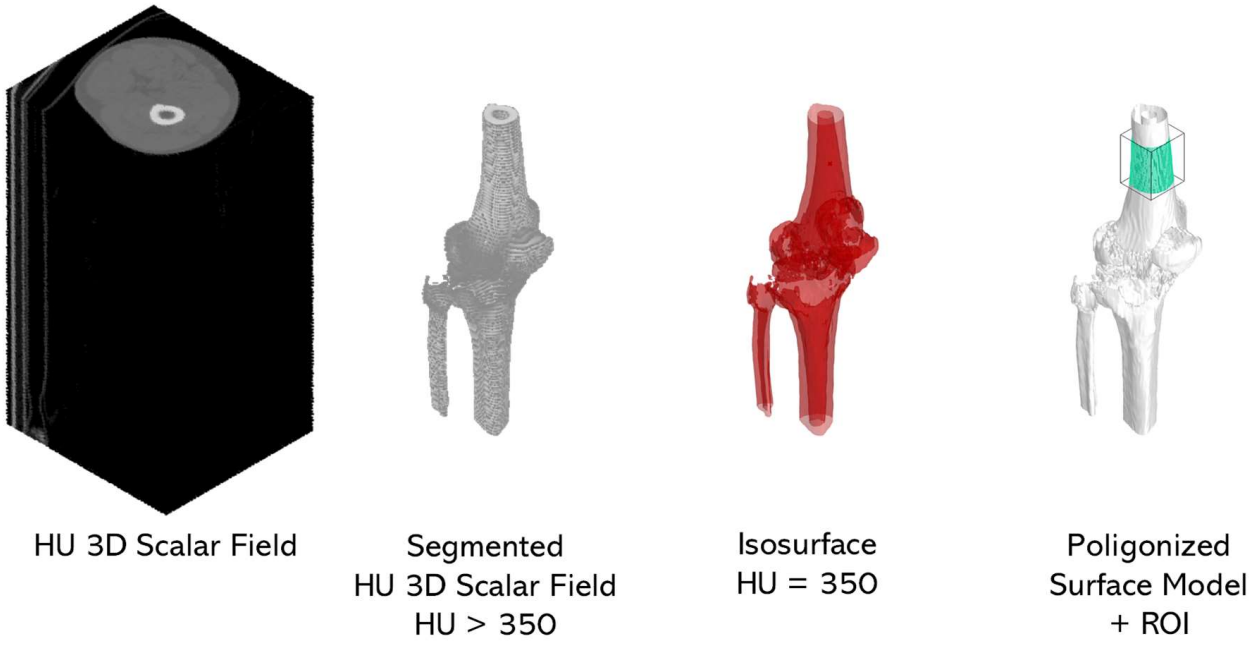

Figure 9. Visualization of the HU 3D scalar field [−1000–1562] in HUs (segmented bone tissue > 350 HU, isosurface at 350 HUs, and polygonized surface model + ROI).

The polygonized surface model was then extracted and the main steps of the process are shown in Figure 9, where the HU 3D scalar field is visualized using a grayscale.

Figure 10 illustrates the main geometrical operations applied to the polygonized surface to isolate a portion of the femur bone, shown in green. The entire polygonized surface is cropped using a Boolean intersection with a box, i.e., the ROI (edges highlighted in red) (Figure 10a). Next, the medullary cavity is closed (Figure 10b). Optionally, a remesh command can be used to refine the polygonized surface (Figure 10c). Finally, the polygonized surface model is exported in .stl file format.

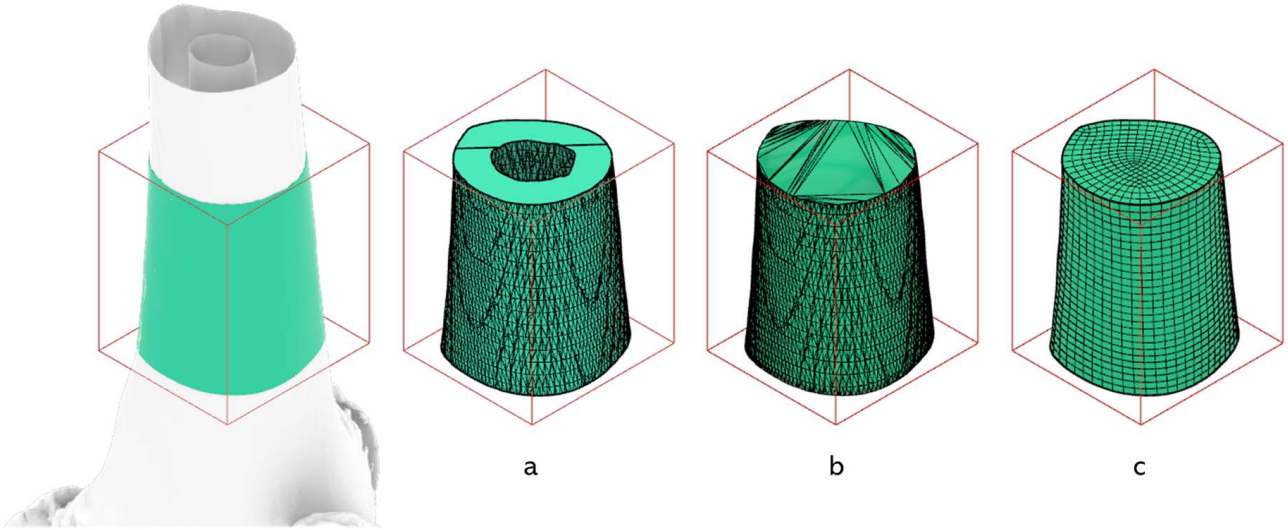

Figure 10. Magnification of the ROI region of the extracted polygonized surface. Shown in green are the femur bone section and geometric modeling steps. The selected femur bone section (**a**), the closed model (**b**), and the final model after quad-remeshing (**c**) are presented.

In this case study, the ROI is a portion of the femur bone, consisting of the cortical bone, trabecular bone, and bone marrow. The bone marrow is contained within the medullary cavity, which is primarily a void, so we consider the highest porosity. The HU–ρ correlation

is derived from the HU_{min} and HU_{max} values of the 3D scalar field inside the femur bone section (−91 to 1516) and the corresponding porosity data from the literature (0.95–0. 1). From this, we can derive the following linear function for the porosity P:

$$P(HU) = -0.000529 \cdot HU + 0.901867, \quad (7)$$

from which we calculate the relative density ρ.

For the generation of the G-code, the .stl file of the polygonized surface model is imported and placed on the print bed in the slicer software, by default in the center touching the bed plane. Table 3 summaries the main process parameters used for the generation of the CAM instructions. Knowing the process limits we previously identified, $E_{w,max}$ is fixed to 1.2 mm at T_{ext} = 215 °C and v_{sp} = 25 mm/s, so L_{cell} = 2.4 mm. For Equation (1) and considering the values in Table 1, ρ_s is set to 0.47.

Table 3. Process parameters for G-code generation.

Process Parameters	Values
Infill type	Gyroid
Infill density, ρ_s	47%
Movement speed, v_{sp}	25 mm/s
Extrusion width, E_w	0.4 mm
Layer thickness, L_{th}	0.2 mm
Number of perimeters	3 (1.2 mm)
Bed temperature, T_{bed}	60/55 °C
Extrusion temperature, T_{ext}	220/215 °C

The CAM instructions are exported in G-code format, while the surface model is saved as a 3D Manufacturing Format (.3mf) file, which contains information about the absolute position of the model in 3D space [55]. Then, the .3mf file is imported in the Rhinoceros/Grasshopper environment.

Figure 5, as previously shown, illustrates the alignment step. Two bounding boxes are constructed over the two geometric surface models—one for the surfaces extracted from the segmentation or polygonization process and cropped by the ROI box, and the other for the surface imported from the slicer software. We identify corresponding points on both bounding boxes, and in this case, we define the translation vector $\overline{v}$, which is:

$$\vec{v} = (130.14,\ 131.86,\ 0) - (69.53,\ 249.60,\ 759.99) = (60.62, -117.74,\ 759.99)$$

Afterward, the G-code is imported into the Grasshopper environment, parsed, and modified using the custom-developed Python script. The modified G-code is then saved and sent to the FFF 3D printer. Figure 11a shows the 3D-printed result.

Although the adopted nominal gyroid cell divides space into two distinct subdomains, the actual fabricated scaffold includes openings that connect these subdomains (see Figure 3a). While subdomains may become effectively disconnected only at higher extrusion widths—a situation that can happen when working with gradients—we were not, however, working with closed cells. This may have been the case for the printed sample (Figure 11b); the interconnectivity between the two subdomains was seemingly preserved at the lower relative density (Figure 11c) but compromised at the higher relative density (Figure 11d). However, regions with higher relative density are usually connected by open channels to less dense areas, ensuring overall interconnectivity. Moreover, by removing the wall during slicing, it is possible to reveal channels similar to Volkmann's canals.

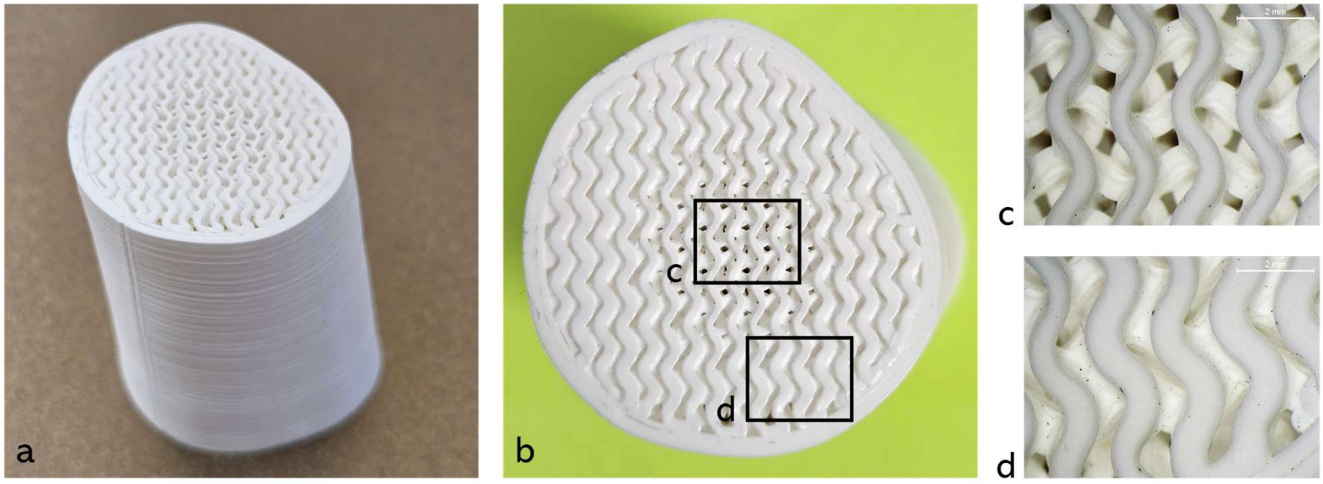

Figure 11. (**a**) An image of the 3D-printed femur segment. (**b**) A top-down view, with magnified insets showing (**c**) the central region and (**d**) an area near the segment's outer boundary (higher relative density).

Despite the proposed method's results shown in the case study, it is important to note that it is not without its limitations, which require further investigation. For instance, it may happen that the values of the 3D scalar field are not adequately suited for the FFF AM process, such as lacking the desired gradient, so several modifications can be applied to adjust these values. Potential approaches include using filtering functions to smooth the data or applying functions to enforce minimum and maximum limits. These adjustments can help fine-tune the scaffold's graded design, ensuring the desired properties and characteristics are achieved. Furthermore, while it is feasible to obtain a low-density structure by controlling the extrusion width and cell size, and optionally the layer height, 100% dense structures are not always attainable. As highlighted in the literature [56,57], there is a delay in deposition; the actual change in the extruded material is offset relative to the corresponding G-code command. This delay arises from complex interactions involving the material properties, material flow, heat transfer, and elasticity, which lead to discrepancies between the intended design and the printed part. Using a direct-drive extruder, as we did, decreases the presence of delay, since the distance between the motor and the heating system is reduced. Figure 12 illustrates this phenomenon in the case study.

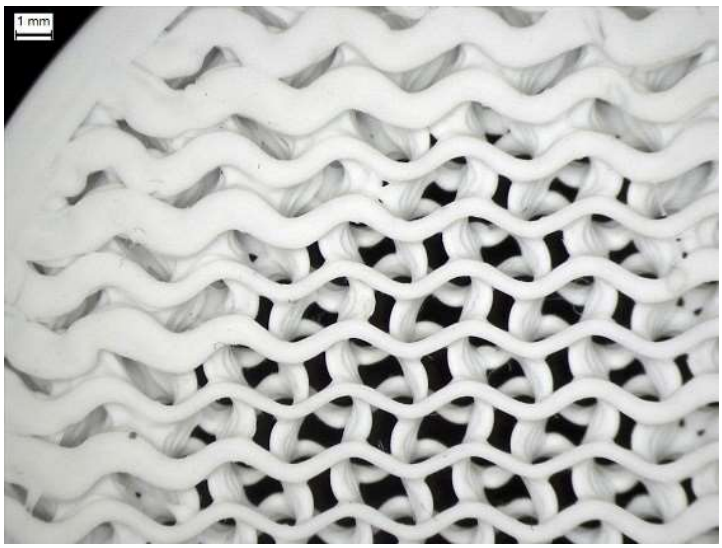

Figure 12. Magnification of femur sample with the first 10 layers (top view).

Furthermore, the effect becomes more evident depending on the order of the commands. Assuming a constant motion speed, transitioning from high to low extrusion rates may be more detrimental than the reverse. This is due to the higher backpressure that builds up in the nozzle during high extrusion rates. When the extrusion rate suddenly decreases, this residual backpressure causes excess material to be extruded, as the system seeks to relieve the pressure. As a result, this behavior limits the ability to create sharp transitions during extrusion. Rapid changes in the extrusion rate inherently introduce gradients, making it difficult to achieve discrete transitions without implementing additional strategies (such as retraction commands) that account for the material's behavior within the nozzle. Nevertheless, even when a slight shift in deposition occurs, the overall relative density of the printed part remains unchanged [42].

The design of lattice structures is constrained by the infill patterns available in each slicer software. These patterns are software-dependent, meaning that the options and implementation may vary across different platforms—even though many slicers (such as Slic3r, PrusaSlicer, Cura, and IceSL) offer similar standard infill types [58,59]. When customizing infill patterns, some slicers such as Cura allow the customization of 2D patterns. While others, such as IceSL, offer 3D pattern capabilities [60], these are not always straightforward or may require workarounds [61]. Plugins and tools within CAD software also exist to generate G-code. One example is the Rhinoceros/Grasshopper add-on Silkworm, among many others, which utilizes curves and polylines as inputs. Alternatively, it should be possible to develop a custom slicer.

The absence of a CAD model for the lattice structure limits its applicability in computer-aided engineering (CAE) analyses. This characteristic identifies the proposed method as CAM-oriented, as the actual design is embedded within the G-code and defined through the control of process parameters rather than explicit geometric modeling. Nevertheless, the volumetric model and homogenization approach can estimate the mechanical behavior of the graded lattice, by treating the bone as a continuum where the mechanical properties depend on the porosity, avoiding the complexities of modeling intricate lattice structures [62–64]. From this perspective, the precise definition of a singular or multiple representative volume elements (RVEs), which are conceptual volumes statistically representative of the effective material properties, is of considerable importance to define the mechanical properties as a function of the porosity via experiments or a finite element (FE) analysis [65].

In addition to the mechanical properties, another important aspect to consider in future research studies is the biological performance of the scaffold. By carefully selecting PLA—or other materials with bioactive or bioresorbable properties and specific characteristics—it is possible to control the degradation rate of the scaffold [17,66,67]. This would let us, for instance, speed up the process in denser areas of the printed scaffold that might have poor interconnections. Lastly, the methodology presented here could be extended to:

- compensate for deposition delay, through a model that considers the variations in pressure due to flow rate changes;
- enlarge the infill database to other TPMS structures or custom patterns, such as patterns conforming to the 3D scalar field or the surface boundaries;
- modify other process parameters such as the temperature and material ratio;
- expand the method to different nozzle diameters such as 0.5 and 0.8 mm;
- mechanically and biologically characterize the 3D components.

This method represents a workaround, although volumetric modifiers should be added in slicer software to permit this type of design modification in the manufactured component.

4. Conclusions

The continuous development of AM technologies highlights the growing need for the efficient management of design and process complexities. This paper presents an alternative approach for modeling and fabricating variable-density lattice structures via MEX FFF, aiming to contribute to both the research and practice. The method integrates geometric modeling and CAM processing into a unified workflow, simplifying challenges such as lattice generation, data exchange, and downstream processing.

The key distinction of the proposed method compared to standard AM workflows lies in the elimination of the need for a CAD model of the lattice structure. Instead, all information related to the local density is directly embedded into a modified G-code file.

In this approach, only a single 3D solid model of the object is needed. The main operations take place directly on the control machine file, i.e., the G-code file. By modifying the infill parameters, the lattice structure is generated and controlled. By utilizing the relative densities derived from CT HU values, the thickness of the infill lattice is locally adapted to match the tissue's actual porosity.

The proposed method offers several advantages. First, it eliminates the need for an explicit geometric model of the lattice; the lattice is directly generated as an infill pattern during slicing, enabling straightforward G-code generation and reducing the risk of inconsistent toolpaths. Second, the overall design-to-fabrication process requires fewer files and fewer steps compared to standard workflows, significantly reducing the modeling effort and minimizing issues related to file exchange. Furthermore, this approach leads to time savings while producing efficient G-code and consistent components.

Author Contributions: Conceptualization, L.G. and G.S.; methodology, L.G. and G.S.; software, L.G. and G.S.; validation, G.S.; formal analysis, L.G.; investigation, L.G.; resources, G.S.; data curation, L.G.; writing—original draft preparation, L.G.; writing—review and editing, L.G. and G.S.; visualization, L.G.; supervision, G.S.; project administration, G.S.; funding acquisition, G.S. All authors have read and agreed to the published version of the manuscript.

Funding: This work was supported by the project "GOALS, Green Optimization by Additive-Manufactured Lightweight Structures", project 20228PFA89, CUP master J53D23001980006, CUP C53D23001670006; and Progetti di Ricerca di Rilevante Interesse Nazionale PRIN 2022, funded under the National Recovery and Resilience Plan (NRRP), Mission 4 Component C2 Investment 1.1 by the European Union—Next-Generation EU.

Institutional Review Board Statement: Not applicable.

Informed Consent Statement: Not applicable.

Data Availability Statement: The original contributions presented in this study are included in the article. Further inquiries can be directed to the corresponding author.

Conflicts of Interest: The authors declare no conflicts of interest.

Abbreviations

The following abbreviations are used in this manuscript:

AM	Additive Manufacturing
CAD	Computer-Aided Design
CAE	Computer-Aided Engineering
CAM	Computer-Aided Manufacturing
CT	Computed Tomography
DICOM	Digital Imaging and Communication in Medicine
DLP	Digital Light Processing

FE	Finite Element
FFF	Fused Filament Fabrication
GAG	Glycosaminoglycans
HA	Hydroxyapatite
HU	Hounsfield Unit
MEX	Material Extrusion
MRI	Magnetic Resonance Imaging
nHA	Nano-Hydroxyapatite
PCL	Polycaprolactone
PET	Positron Emission Tomography
PGA	Polyglycolic Acid
PLA	Polylactic Acid
PLLA	Poly-l-Lactic Acid
ROI	Region of Interest
RVE	Representative Volume Element
SLM	Selective Laser Melting
SLS	Selective Laser Sintering
TPMS	Triply Periodic Minimal Surface
TCP	Tricalcium Phosphate
VPP	Vat Photopolimerization

References

1. Eltom, A.; Zhong, G.; Muhammad, A. Scaffold Techniques and Designs in Tissue Engineering Functions and Purposes: A Review. *Adv. Mater. Sci. Eng.* **2019**, *2019*, 3429527. [CrossRef]
2. Kumar, A.; Jacob, A. Techniques in scaffold fabrication process for tissue engineering applications: A review. *J. Appl. Biol. Biotechnol.* **2022**, *10*, 163–176. [CrossRef]
3. Varghese, M.G.; Thomas, A.; Rupesh, S.; Sameer, K.M.; Joseph, D.; Thomas, N.G. Fabrication Techniques for Scaffolds Applied in Regenerative Medicine. In *Novel Biomaterials for Tissue Engineering*; Vizureanu, P., Baltatu, M.S., Eds.; IntectOpen: London, UK, 2024. [CrossRef]
4. Subramaniyan, M.; Eswaran, P.; Appusamy, A.; Srimannarayana Raju, P.S.; Rahini, V.; Madhumitha, T.R.; Thisha, R. A survey on applications of additive manufacturing techniques in tissue engineering. *Mater. Today Proc.* **2021**, *45*, 8036–8040. [CrossRef]
5. Ożóg, P.; Elsayed, H.; Grigolato, L.; Savio, G.; Kraxner, J.; Galusek, D. Bernardo E: Engineering of silicone-based blends for the masked stereolithography of biosilicate/carbon composite scaffolds. *J. Eur. Ceram. Soc.* **2022**, *42*, 6192–6198. [CrossRef]
6. Elsayed, H.; Secco, M.; Zorzi, F.; Schuhladen, K.; Detsch, R.; Boccaccini, A.R.; Bernardo, E. Highly Porous Polymer-Derived Bioceramics Based on a Complex Hardystonite Solid Solution. *Materials* **2019**, *12*, 3970. [CrossRef]
7. Zafar, M.J.; Zhu, D.; Zhang, Z. 3D Printing of Bioceramics for Bone Tissue Engineering. *Materials* **2019**, *12*, 3361. [CrossRef]
8. Liu, Y.-Y.; Echeverry-Rendón, M. 3D-printed biodegradable polymer scaffolds for tissue engineering: An overview, current stage and future perspectives. *Next Mater.* **2025**, *8*, 100647. [CrossRef]
9. NEMA. DICOM PS3.1 2021e—Introduction and Overview. Available online: https://dicom.nema.org/medical/Dicom/2021e/output/chtml/part01/PS3.1.html (accessed on 10 December 2024).
10. *ISO 12052:2017*; Health Informatics—Digital Imaging and Communication in Medicine (DICOM) Including Workflow and Data Management (EN). ISO: Geneva, Switzerland, 2017.
11. DenOtter, T.D.; Schubert, J. *Hounsfield Unit*; StatPearls: Petersburg, FL, USA, 2025.
12. Lamba, R.; McGahan, J.P.; Corwin, M.T.; Li, C.-S.; Tran, T.; Seibert, J.A.; Boone, J.M. CT Hounsfield Numbers of Soft Tissues on Unenhanced Abdominal CT Scans: Variability Between Two Different Manufacturers' MDCT Scanners. *Am. J. Roentgenol.* **2014**, *203*, 1013–1020. [CrossRef]
13. Hurrell, M.A.; Butler, A.P.H.; Cook, N.J.; Butler, P.H.; Ronaldson, J.P.; Zainon, R. Spectral Hounsfield units: A new radiological concept. *Eur. Radiol.* **2012**, *22*, 1008–1013. [CrossRef]
14. Bazalova, M.; Carrier, J.-F.; Beaulieu, L.; Verhaegen, F. Dual-energy CT-based material extraction for tissue segmentation in Monte Carlo dose calculations. *Phys. Med. Biol.* **2008**, *53*, 2439–2456. [CrossRef]
15. Amini, I.; Akhlaghi, P. Evaluation of CT calibration curves from stoichiometric and tissue substitute methods according to tissue characteristics. *Radioprotection* **2019**, *54*, 117–123. [CrossRef]
16. Mukasheva, F.; Adilova, L.; Dyussenbinov, A.; Yernaimanova, B.; Abilev, M.; Akilbekova, D. Optimizing scaffold pore size for tissue engineering: Insights across various tissue types. *Front. Bioeng. Biotechnol.* **2024**, *12*, 1444986. [CrossRef] [PubMed]

17. Ito, M.; Okamoto, M. Structure and properties of 3D resorbable scaffolds based on poly(L-lactide) via salt-leaching combined with phase separation. *Int. J. Hydrol.* **2023**, *7*, 73–76. [CrossRef]
18. Ashby, M.F. The properties of foams and lattices. *Philos. Trans. R. Soc. A Math. Phys. Eng. Sci.* **2006**, *364*, 15–30. [CrossRef]
19. Veloso, F.; Gomes-Fonseca, J.; Morais, P.; Correia-Pinto, J.; Pinho, A.C.M.; Vilaça, J.L. Overview of Methods and Software for the Design of Functionally Graded Lattice Structures. *Adv. Eng. Mater.* **2022**, *24*, 2200483. [CrossRef]
20. Savio, G.; Rosso, S.; Meneghello, R.; Concheri, G. Geometric Modeling of Cellular Materials for Additive Manufacturing in Biomedical Field: A Review. *Appl. Bionics Biomech.* **2018**, *2018*, 1654782. [CrossRef]
21. Dasan, A.; Elsayed, H.; Kraxner, J.; Galusek, D. Bernardo E: Hierarchically porous 3D-printed akermanite scaffolds from silicones and engineered fillers. *J. Eur. Ceram. Soc.* **2019**, *39*, 4445–4449. [CrossRef]
22. Leonardi, F.; Graziosi, S.; Casati, R.; Tamburrino, F.; Bordegoni, M. Additive Manufacturing of Heterogeneous Lattice Structures: An Experimental Exploration. *Proc. Des. Soc. Int. Conf. Eng. Des.* **2019**, *1*, 669–678. [CrossRef]
23. Savio, G.; Meneghello, R.; Concheri, G. Geometric modeling of lattice structures for additive manufacturing. *Rapid Prototyp. J.* **2018**, *24*, 351–360. [CrossRef]
24. Barba, D.; Alabort, E.; Reed, R.C. Synthetic bone: Design by additive manufacturing. *Acta Biomater.* **2019**, *97*, 637–656. [CrossRef]
25. Ataollahi, S. A review on additive manufacturing of lattice structures in tissue engineering. *Bioprinting* **2023**, *35*, e00304. [CrossRef]
26. Bracaglia, L.G.; Smith, B.T.; Watson, E.; Arumugasaamy, N.; Mikos, A.G.; Fisher, J.P. 3D printing for the design and fabrication of polymer-based gradient scaffolds. *Acta Biomater.* **2017**, *56*, 3–13. [CrossRef]
27. Van Bael, S.; Kerckhofs, G.; Moesen, M.; Pyka, G.; Schrooten, J.; Kruth, J.P. Micro-CT-based improvement of geometrical and mechanical controllability of selective laser melted Ti6Al4V porous structures. *Mater. Sci. Eng. A* **2011**, *528*, 7423–7431. [CrossRef]
28. Van Bael, S.; Chai, Y.C.; Truscello, S.; Moesen, M.; Kerckhofs, G.; Van Oosterwyck, H.; Kruth, J.-P.; Schrooten, J. The effect of pore geometry on the in vitro biological behavior of human periosteum-derived cells seeded on selective laser-melted Ti6Al4V bone scaffolds. *Acta Biomater.* **2012**, *8*, 2824–2834. [CrossRef] [PubMed]
29. Zhang, X.-Y.; Fang, G.; Leeflang, S.; Zadpoor, A.A.; Zhou, J. Topological design, permeability and mechanical behavior of additively manufactured functionally graded porous metallic biomaterials. *Acta Biomater.* **2019**, *84*, 437–452. [CrossRef] [PubMed]
30. Warnke, P.H.; Douglas, T.; Wollny, P.; Sherry, E.; Steiner, M.; Galonska, S.; Becker, S.T.; Springer, I.N.; Wiltfang, J.; Sivananthan, S. Rapid Prototyping: Porous Titanium Alloy Scaffolds Produced by Selective Laser Melting for Bone Tissue Engineering. *Tissue Eng. Part C Methods* **2009**, *15*, 115–124. [CrossRef]
31. Taniguchi, N.; Fujibayashi, S.; Takemoto, M.; Sasaki, K.; Otsuki, B.; Nakamura, T.; Matsushita, T.; Kokubo, T.; Matsuda, S. Effect of pore size on bone ingrowth into porous titanium implants fabricated by additive manufacturing: An in vivo experiment. *Mater. Sci. Eng. C* **2016**, *59*, 690–701. [CrossRef]
32. Fukuda, A.; Takemoto, M.; Saito, T.; Fujibayashi, S.; Neo, M.; Pattanayak, D.K.; Matsushita, T.; Sasaki, K.; Nishida, N.; Kokubo, T.; et al. Osteoinduction of porous Ti implants with a channel structure fabricated by selective laser melting. *Acta Biomater.* **2011**, *7*, 2327–2336. [CrossRef]
33. Guo, W.; Li, P.; Pang, Y.; Wang, E.; Zhao, L.; Huang, Y.; Wang, S.; Liu, B.; You, H.; Long, Y. Biomimetic TPMS porous hydroxyapatite bone scaffolds doped with bioactive glass: Digital light processing additive manufacturing, microstructure and performance. *Compos. Part A Appl. Sci. Manuf.* **2025**, *193*, 108870. [CrossRef]
34. Zhang, B.; Wang, L.; Song, P.; Pei, X.; Sun, H.; Wu, L.; Zhou, C.; Wang, K.; Fan, Y.; Zhang, X. 3D printed bone tissue regenerative PLA/HA scaffolds with comprehensive performance optimizations. *Mater. Des.* **2021**, *201*, 109490. [CrossRef]
35. Okkalidis, N. A novel 3D printing method for accurate anatomy replication in patient-specific phantoms. *Med. Phys.* **2018**, *45*, 4600–4606. [CrossRef] [PubMed]
36. Yau, H.-T.; Chen, Q.-F.; Huang, H.-Y.; Vu-Dinh, H. From computed tomography to 3D printed heterogeneous scaffolds: A novel approach to simulating bone characteristics using octree adaptive subdivision. *Mater. Des.* **2024**, *245*, 113277. [CrossRef]
37. Ranellucci, A. Slic3r. Available online: https://slic3r.org/ (accessed on 14 January 2020).
38. Sedničková, M.; Pekařová, S.; Kucharczyk, P.; Bočkaj, J.; Janigová, I.; Kleinová, A.; Jochec-Mošková, D.; Omaníková, L.; Perd'ochová, D.; Koutný, M.; et al. Changes of physical properties of PLA-based blends during early stage of biodegradation in compost. *Int. J. Biol. Macromol.* **2018**, *113*, 434–442. [CrossRef] [PubMed]
39. Annex, A. ID Listings, Medium, Density, Mass, Minimum/Maximum Columns, Rows and Slices Occupied by Each Organ/Tissue (Containing Rectangular Prism), and Organ Centres of Mass. In *Annals of the ICRP*; Sage: Thousand Oaks, CA, USA, 2009; Volume 39, pp. 47–70. [CrossRef]
40. Ma, X.; Figl, M.; Unger, E.; Buschmann, M.; Homolka, P. X-ray attenuation of bone, soft and adipose tissue in CT from 70 to 140 kV and comparison with 3D printable additive manufacturing materials. *Sci. Rep.* **2022**, *12*, 14580. [CrossRef]
41. Bourke, P. Polygonising a Scalar Field. Available online: https://paulbourke.net/geometry/polygonise/ (accessed on 10 December 2024).
42. Grigolato, L.; Rosso, S.; Meneghello, R.; Concheri, G.; Savio, G. Design and manufacturing of graded density components by material extrusion technologies. *Addit. Manuf.* **2022**, *57*, 102950. [CrossRef]

43. Acierno, D.; Patti, A. Fused Deposition Modelling (FDM) of Thermoplastic-Based Filaments: Process and Rheological Properties—An Overview. *Materials* **2023**, *16*, 7664. [CrossRef] [PubMed]
44. Turner, B.N.; Gold, S.A. A review of melt extrusion additive manufacturing processes:, II. Materials, dimensional accuracy, and surface roughness. *Rapid Prototyp. J.* **2015**, *21*, 250–261. [CrossRef]
45. *ISO: ISO 6983-1:2009*; Automation Systems and Integration—Numerical Control of Machines—Program Format and Definitions of Address Words—Part 1: Data Format for Positioning, Line Motion and Contouring Control Systems. ISO: Geneva, Switzerland, 2009.
46. Morgan, E.F.; Unnikrisnan, G.U.; Hussein, A.I. Bone Mechanical Properties in Healthy and Diseased States. *Annu. Rev. Biomed. Eng.* **2018**, *20*, 119–143. [CrossRef]
47. Cooper, D.M.L.; Kawalilak, C.E.; Harrison, K.; Johnston, B.D.; Johnston, J.D. Cortical Bone Porosity: What Is It, Why Is It Important, and How Can We Detect It? *Curr. Osteoporos. Rep.* **2016**, *14*, 187–198. [CrossRef]
48. Boughton, O.R.; Ma, S.; Cai, X.; Yan, L.; Peralta, L.; Laugier, P.; Marrow, J.; Giuliani, F.; Hansen, U.; Abel, R.L.; et al. Computed tomography porosity and spherical indentation for determining cortical bone millimetre-scale mechanical properties. *Sci. Rep.* **2019**, *9*, 7416. [CrossRef]
49. Lim Fat, D.; Kennedy, J.; Galvin, R.; O'Brien, F.; Mc Grath, F.; Mullett, H. The Hounsfield value for cortical bone geometry in the proximal humerus—An in vitro study. *Skelet. Radiol.* **2012**, *41*, 557–568. [CrossRef]
50. Porrelli, D.; Abrami, M.; Pelizzo, P.; Formentin, C.; Ratti, C.; Turco, G.; Grassi, M.; Canton, G.; Grassi, G. Murena L: Trabecular bone porosity and pore size distribution in osteoporotic patients—A low field nuclear magnetic resonance and microcomputed tomography investigation. *J. Mech. Behav. Biomed. Mater.* **2022**, *125*, 104933. [CrossRef]
51. Bala, Y.; Zebaze, R.; Seeman, E. Role of cortical bone in bone fragility. *Curr. Opin. Rheumatol.* **2015**, *27*, 406–413. [CrossRef] [PubMed]
52. Teng, Y.-C.; Chen, J.; Zhong, W.-B.; Liu, Y.-H. Construct a Refined Monte Carlo Model for BNCT Dose Calculation and Assessment by Converting HU Value to Material Compositions for ROIs. *Res. Sq.* **2024**. [CrossRef]
53. Bourke, P. Trilinear Interpolation. Available online: https://paulbourke.net/miscellaneous/interpolation/ (accessed on 10 December 2024).
54. Knee and Bones 1.0.0. Available online: https://www.embodi3d.com/files/file/19722-knee-and-bones/ (accessed on 10 February 2022).
55. 3mf Specifications. Available online: https://3mf.io/spec/ (accessed on 18 February 2025).
56. Bellini, A.; Güçeri, S.; Bertoldi, M. Liquefier Dynamics in Fused Deposition. *J. Manuf. Sci. Eng.* **2004**, *126*, 237–246. [CrossRef]
57. Turner, B.N.; Strong, R.; Gold, S.A. A review of melt extrusion additive manufacturing processes: I. Process design and modeling. *Rapid Prototyp. J.* **2014**, *20*, 192–204. [CrossRef]
58. Ultimaker: Cura Infill Settings. Available online: https://support.ultimaker.com/s/article/1667411002588 (accessed on 13 December 2024).
59. Prusa Research: Infill Patterns. Available online: https://help.prusa3d.com/article/infill-patterns_177130 (accessed on 13 December 2024).
60. Tricard, T.; Tavernier, V.; Zanni, C.; Martínez, J.; Hugron, P.-A.; Neyret, F.; Lefebvre, S. Freely orientable microstructures for designing deformable 3D prints. *ACM Trans. Graph.* **2020**, *39*, 1–16. [CrossRef]
61. Custom Infill Shape? Available online: https://www.reddit.com/r/Cura/comments/pvb427/custom_infill_shape/ (accessed on 20 May 2025).
62. Savio, G.; Curtarello, A.; Rosso, S.; Meneghello, R. Concheri G: Homogenization driven design of lightweight structures for additive manufacturing. *Int. J. Interact. Des. Manuf.* **2019**, *13*, 263–273. [CrossRef]
63. Freund, J.; Karakoç, A.; Sjölund, J. Computational homogenization of regular cellular material according to classical elasticity. *Mech. Mater.* **2014**, *78*, 56–65. [CrossRef]
64. Dong, G.; Tang, Y.; Zhao, Y.F. A Survey of Modeling of Lattice Structures Fabricated by Additive Manufacturing. *J. Mech. Des.* **2017**, *139*, 100906. [CrossRef]
65. Gonabadi, H.; Chen, Y.; Bull, S. Investigation of the effects of volume fraction, aspect ratio and type of fibres on the mechanical properties of short fibre reinforced 3D printed composite materials. *Prog. Addit. Manuf.* **2025**, *10*, 261–277. [CrossRef]
66. Ma, P.X. Scaffolds for tissue fabrication. *Mater. Today* **2004**, *7*, 30–40. [CrossRef]
67. Stratton, S.; Shelke, N.B.; Hoshino, K.; Rudraiah, S.; Kumbar, S.G. Bioactive polymeric scaffolds for tissue engineering. *Bioact. Mater.* **2016**, *1*, 93–108. [CrossRef] [PubMed]